

## Research Article

# Application of Single and Dual Multilayer Optics for Powder X-Ray Diffraction

**Scott T. Misture**

*Kazuo Inamori School of Engineering, Alfred University, Alfred, NY 14802, USA*

Correspondence should be addressed to Scott T. Misture, [misture@alfred.edu](mailto:misture@alfred.edu)

Received 24 February 2008; Accepted 18 June 2008

Recommended by Walter Gibson

The performance of parallel beam multilayer optics, including a parabolic multilayer Osmic MaxFlux GO-13N and a flat custom multilayer, was evaluated experimentally and compared to Bragg-Brentano and traditional “parallel beam” or “thin film” optical geometries. A novel arrangement of a parabolic multilayer in the incident beam with a flat multilayer in the diffracted beam functioning as an analyzer crystal was proven effective for powder diffraction applications. The dual-optic configuration improves resolution while eliminating sample displacement and transparency errors as expected for a configuration with equatorial divergence below 100 arcseconds. Fundamental parameters fitting showed that the parabolic multilayer can be accurately modeled using a constant Gaussian function, while a long parallel-plate soller collimator requires a constant hat function. No additional convolutions are necessary for the diffracted-beam flat multilayer because of the lower acceptance angle.

Copyright © 2008 Scott T. Misture. This is an open access article distributed under the Creative Commons Attribution License, which permits unrestricted use, distribution, and reproduction in any medium, provided the original work is properly cited.

## 1. Introduction

Powder diffraction broadly encompasses many measurements; powder diffraction, thin film diffraction, diffuse and specular reflectivity, residual stress, and texture analysis among them. Of these measurements, powder diffraction, thin film diffraction, and reflectivity are routinely performed using  $\Theta$ - $2\Theta$  diffractometers with appropriate attachments and optics. The incorporation of parabolic multilayer optics for powder diffraction has been studied by several groups, with varied results that depend upon the particular application [1–9]. Research to date has focused mainly on the use of a parabolic multilayer in the incident beam to collimate the beam, with diffracted-side optics that include either a long soller parallel-plate collimator or collimator with crystal combination [4, 6, 8, 10, 11]. Additional studies focus on the use of parabolic multilayers to couple with 2- or 4-bounce channel cut crystal monochromators [7, 12], and dual mirror combinations where a secondary parabolic multilayer is used as an analyzer crystal [13].

Ray tracing calculations for prediction of intensities and diffraction geometries by Toraya and Hibino [9] as well as by Gutman and Verman [3] demonstrate that one should expect a shift in the  $\alpha_1$  and  $\alpha_2$  peak separations as a result of slightly

different diffraction angles from the multilayer. Of course, the different diffraction angles for the  $\alpha_1$  and  $\alpha_2$  radiation are not an issue if one employs a channel-cut monochromator to further condition the beam.

Applications of parallel beam systems for powder and thin film diffraction, either using parallel-plate collimators or multilayers, are reasonably well established. A recent paper [8] compared the use of a single parabolic multilayer with cross-coupled (Kirkpatrick-Baez) multilayers, and clearly demonstrated that the incident beam parabolic multilayer is well-suited for the study of very thin films. The present paper focuses on the use of a dual-multilayer configuration for powder diffraction, however, with a novel arrangement that includes a parabolic multilayer on the incident side and a flat multilayer as an analyzer crystal.

## 2. Experimental procedures

A Siemens D-500 diffractometer, fitted with a Cu line-focus tube, scintillation counter, and 200 mm radius, was used in all of the measurements. Five diffraction geometries were used for the comparisons. All experiments were run as step scans, using  $0.02^\circ$  step size and 2-second count times with

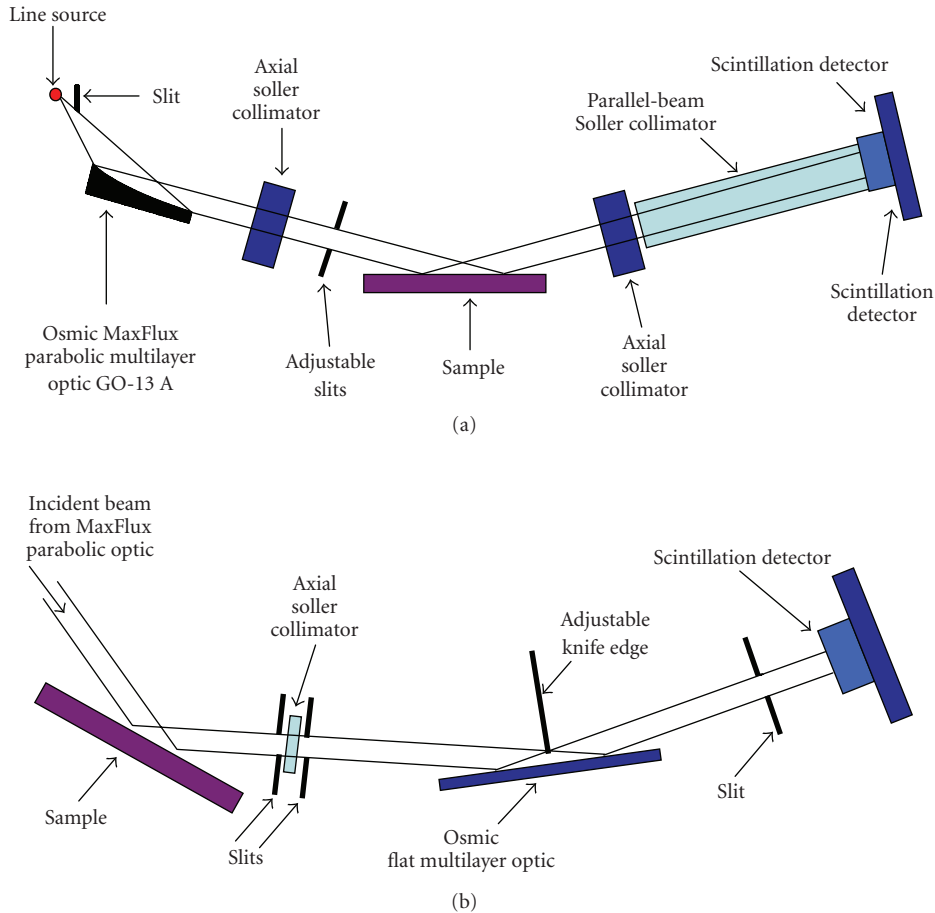


FIGURE 1: Schematic of the beam configurations tested, including (a) a single parabolic multilayer in ++ arrangement, and (b) the novel dual multilayer configuration in the +++ configuration.

the X-ray tube running at 1200 W. Each powder specimen was mounted in a 15 × 15 mm side-drifted sample holder. In all cases, axial collimation was provided by a 3° collimator in the incident beam side.

The instrumental arrangements included the following.

*Bragg-Brentano (BB)* geometry with 1° divergence slits, 0.05 mm receiving slit, 6° tube takeoff angle, diffracted-beam graphite monochromator, and 13 mm diameter detector aperture. All measurements were made as coupled  $\Theta$ -2 $\Theta$  step scans.

*Parallel-Beam (PB)* geometry using 2 $\Theta$  scans with  $\Theta$  fixed at 2.0°. The (P-B) arrangement included divergence slits set to 0.14° to illuminate 15 mm of the specimen at  $\Theta = 2^\circ$ . A thin film attachment (long Sollor collimator) with divergence of 0.15° was installed on the diffracted beam side of the diffractometer, with a detector aperture 13 mm in diameter. A Ni beta filter 0.03 mm thick was installed on the diffracted beam side of the diffractometer as the only energy discrimination.

*Parabolic Multilayer (PM)*. An Osmic MaxFlux optic (GO-13N) was installed in a modified Huber monochromator housing (see Figure 1), while the diffracted beam side included the 0.15° thin film attachment and a detector

aperture 13 mm in diameter. The multilayer and sample were arranged in either ++ or +- configurations. The GO-13 is characterized by an average reflectivity of 66% for Cu radiation with physical dimensions of 40 by 20 mm. No beta filter was used. 2 $\Theta$  scans were made with  $\Theta$  fixed at 3.6° or as coupled measurements, as noted below. Because the optic provides a beam which is ~0.9 mm in height, the  $\Theta$  angle was chosen to illuminate 14 mm of the 15 mm powder samples when illuminating the sample at 3.6° $\Theta$ .

*Parabolic incident multilayer and diffracted-beam flat multilayer (PM+FM)*. This arrangement is shown in Figure 1 and includes a flat multilayer in the diffracted beam side. The flat multilayer was produced by Osmic, Inc., Mich, USA, with physical dimensions of 32 by 65 mm and average reflectivity for Cu radiation of 72%. The rocking curve width on average is 96 arcseconds. Measurements were made using either coupled  $\Theta$ -2 $\Theta$  scans or with  $\Theta$  fixed at 3.6°, such that the entire beam (~0.8 × 12 mm) illuminated the 15 mm sample. The multilayers and sample were arranged in either +++ or +-+ configurations.

The samples are listed in Table 1 and include a wide range of absorption coefficients for evaluating sample transparency errors. Each powder sample was loaded into a side-drifted

TABLE 1: Samples used in the investigation.

Sample	Form
Silver	powder
Linde C ( $\alpha$ -Al <sub>2</sub> O <sub>3</sub> )	powder
Urea [CO(NH <sub>2</sub> ) <sub>2</sub> ]	powder
SRM 640b & c Si	powder
SRM 660 LaB <sub>6</sub>	powder
Quartz	50 × 50 mm plate

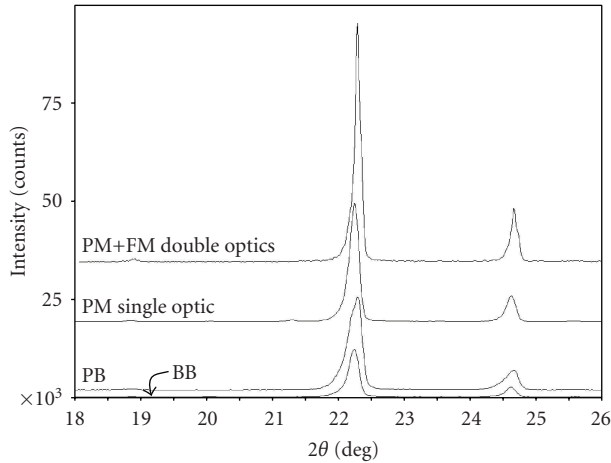


FIGURE 2: Qualitative comparison of data from four optical configurations for a thick powder sample of urea. Data are normalized to a common background intensity and offset vertically for clarity.

powder holder with dimensions 15 mm by 15 mm by 4 mm deep. Data analysis was completed using HighScore [14] and Topas [15].

### 3. Results and discussion

All of the diffraction geometries provided high-quality data within expectations of the optical configurations, as shown for example in Figure 2. The novel arrangement of PM + FM provided data of outstanding quality without any obvious complications. Visual inspection of the range of data naturally demonstrates large differences in resolution and intensity among the various configurations.

A point of concern with multilayer optics is the distortion of the  $K\alpha_1$  and  $K\alpha_2$  beam directions, which has been established both experimentally and by ray tracing calculations [3, 8, 9]. As shown by Toraya and Hibino [9], the spacing between the  $K\alpha_1$  and  $K\alpha_2$  lines is a function of several parameters, most importantly the spectral resolution of the multilayers. These authors used an optical configuration nearly identical to our PM configuration, but with an older-generation longer (150 mm) multilayer. Their work incorporated a high-resolution encoded goniometer; however, the  $\alpha_1/\alpha_2$  separation remained unchanged within the experimental error. Likewise, we were unable to detect abnormal  $\alpha_1/\alpha_2$  separation in any of our measurements,

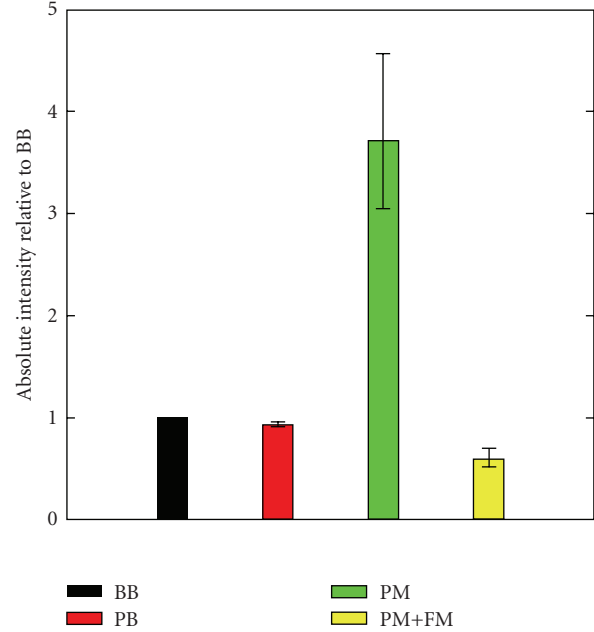


FIGURE 3: Ratio of absolute intensities obtained for each optical configuration.

either PM or PM + FM, in either ++ or +- arrangement for the former or +-+ or +++ for the latter. Both profile fitting and Rietveld analyses were successful without altering the  $\alpha_1/\alpha_2$  separation or intensity ratios, as described in more detail below.

#### 3.1. Intensity

The absolute intensities were compared on a peak-by-peak basis for Ag, alumina, urea, and quartz. The overall average absolute peak intensities were used for the comparisons. Figure 3 shows the absolute intensities relative to the intensity measured in the standard Bragg-Brentano configuration and highlights the improved intensity, of approximately 4 times, in the configuration with the parabolic multilayer and fixed incident angle of  $3.6^\circ$ .

While several authors have used ray tracing calculations to estimate intensities and beam paths with multilayer optics [3, 8, 9], the differences in the measured intensities shown in Figure 3 can be explained qualitatively by considering the beam paths. For example, in the BB geometry,  $\sim 1^\circ$  of divergence is used in the incident and diffracted beams. In stark contrast, the traditional PB measurement includes very fine slits to irradiate a 15 mm sample at an incident angle of  $2^\circ 2\theta$ , or  $\sim 0.14^\circ$  of divergence. Therefore, one would expect substantially fewer photons incident upon the sample, by a factor of  $\sim 7$ , in the PB configuration. Further, to obtain similar measured intensities as shown in Figure 3, the diffracted-beam side optics must pass  $\sim 7$  times more photons than the diffracted-beam graphite monochromator in the BB configuration.

Extending similar arguments to the multilayers, one finds that the parabolic multilayer captures  $\sim 0.5^\circ$  of divergence,

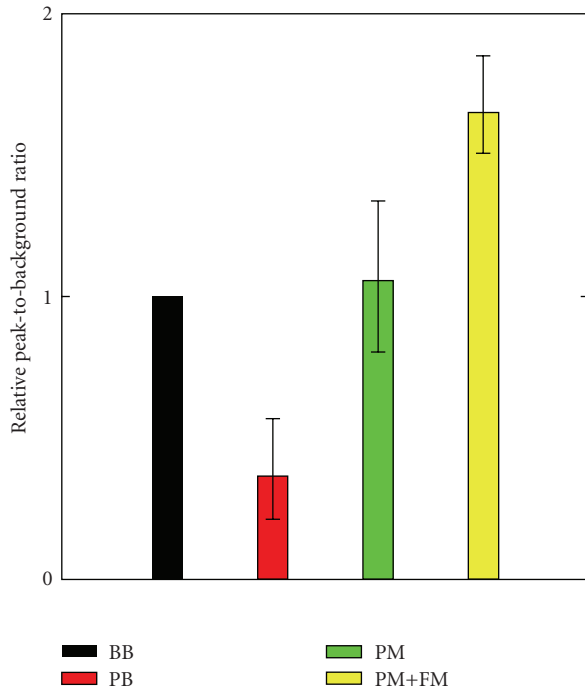


FIGURE 4: Peak-to-background ratios for each configuration relative to the BB configuration.

diffracts  $\sim 65\%$  of the incident radiation, and is equipped with the same diffracted-beam side optics as the PB configuration. Therefore, the total intensity should be on the order of  $\sim 2.5$  times larger than that measured in the BB configuration, a prediction in reasonable agreement with the measured value of 3.8 times, considering minor differences in alignment.

Adding the second multilayer in the diffracted beam side substantially reduces the intensity, but, as shown later, also improves resolution. The second multilayer, with reflectivity of  $\sim 70\%$ , offers approximately the same throughput as a graphite diffracted beam monochromator. However, the multilayer also offers beam collimation that is much tighter than that offered by the long Soller collimator, by a factor of  $\sim 6$  (recall that the rocking curve width of the multilayer is 96 arcseconds, and the long Soller collimator has divergence of  $\sim 0.15^\circ$  or 540 arcseconds). Therefore, one can employ the multilayer without a long Soller collimator to achieve parallel beam conditions. The efficiency of the multilayer is close to that of the Soller collimator used here, such that the overall intensity of the PM + FM design is approximately the same as for the PB and BB configurations.

### 3.2. Peak-to-background ratios

The peak-to-background ratios were calculated on a peak-by-peak basis exactly as were the intensity ratios. The results are shown in Figure 4. The BB configuration provides a peak-to-background ratio that is substantially higher than for the PB configuration, about the same as the PM configuration and worse by a factor of  $\sim 0.5$  than the PM +

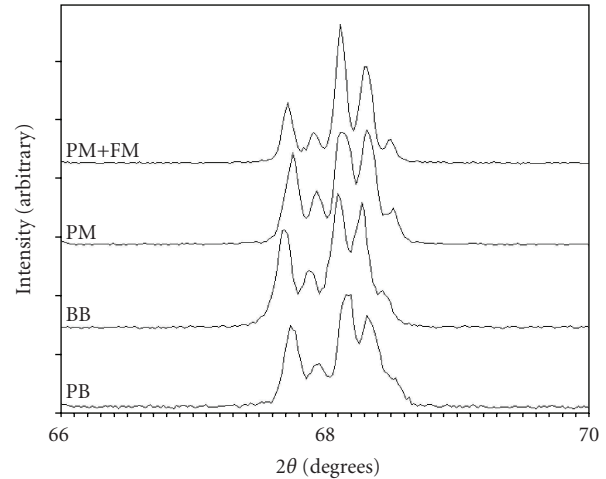


FIGURE 5: Quartz diffraction data for each optical configuration.

FM configuration. One would expect the PB configuration to provide lower peak-to-background ratios because the only energy discrimination in the system is the Ni foil  $K\beta$  filter. In contrast, the PM configuration yields peak-to-background ratios that are more than double those for the PB configuration. Here, one must consider the incident beam spectrum after diffraction from the incident beam parabolic multilayer. Because the multilayer passes only a small window around the  $K\alpha_1$  and  $K\alpha_2$  lines, scattering and fluorescence are reduced before the sample, thus improving the peak-to-background ratio. Adding the second multilayer again provides additional energy discrimination and tight angular acceptance, improving the peak-to-background ratio further.

### 3.3. Resolution

The instrumental resolution was determined using the traditional approach by measuring the “5 fingers” of quartz, as recommended by Jenkins and Snyder [16]. The divergence of the PB, PM, and PM+FM configurations, although “parallel” in comparison to BB optics, is a function of the optics. For the “parallel” configurations, the incident/diffracted beam side divergence is on the order of 540/540 for PB, 96/540 for PM, and 96/96 arcseconds for the PM + FM configurations. Naturally, one expects improved instrumental resolution with lower divergence optics.

Figure 5 shows the diffraction patterns for quartz in the various diffractometer configurations. Calculated resolution values between 1.5 and 2.0, based upon peak-to-valley ratios in the quartz peaks, are the accepted range for “high-resolution” Bragg-Brentano measurements [16]. As shown in Figure 5, the BB configuration resolution value is 1.7, while those for PB, PM, and PM + FM are 1.5, 2.0, and 4.0, respectively. Note that the resolution when using the PM optics is some 20% better than a Bragg-Brentano measurement and  $\sim 40\%$  better than the traditional PB optics. Incorporating the diffracted beam multilayer optic again improves the resolution to a value of 4, as would be

TABLE 2: Refined lattice parameters using uncalibrated peak positions.

Material/configuration	$a$ axis (Å)	$c$ axis (Å)	No. of Peaks indexed	Smith/Snyder $F_N$	No. of ESD from calibrated BB ( $a$ axis/ $c$ axis)	
Ag B-B	4.0878(1)		9	$f(8) = 168$ (0.0060, 8)	10.3	
Ag PB	4.0859(4)		9	$f(8) = 31$ (0.0326, 8)	1.7	
Ag PM	4.0862(3)		9	$f(8) = 49$ (0.0204, 8)	1.2	
Linde C BB	4.7616(2)	12.9993(9)	32	$f(30) = 33$ (0.0204, 44)	11.9	7.6
Linde C PB	4.7591(1)	12.9887(9)	30	$f(30) = 38$ (0.0174, 45)	0.80	4.19
Linde C PM	4.7587(1)	12.9915(7)	30	$f(30) = 46$ (0.0147, 45)	3.47	1.37
Urea BB	5.660(1)	4.712(1)	22	$f(21) = 16$ (0.0261, 50)	13.4	8.90
Urea PB	5.6470(6)	4.706(1)	19	$f(19) = 21$ (0.0281, 32)	0.50	2.9
Urea PM	5.6464(4)	4.701(1)	18	$f(18) = 99$ (0.0057, 32)	0.25	2.10
Urea PM + FM	5.6481(3)	4.702(2)	19	$f(19) = 65$ (0.0051, 58)	1.8	1.5

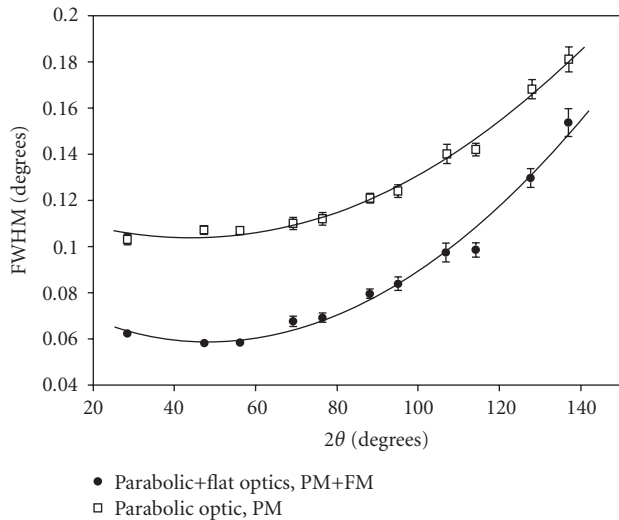


FIGURE 6: Peak FWHM ( $K\alpha_1$ ) for SRM640c Si powder using the PM and PM + FM configurations. Error bars are  $\pm 1$  estimated standard deviation from profile fitting.

expected from the smaller acceptance angle of the diffracted-beam multilayer compared to the Soller collimator.

### 3.4. Profile shapes

Diffraction peak shapes influence all aspects of data analysis, and for low absorption materials measured with Bragg-Brentano geometry, substantial systematic error should be expected. The peak shapes/widths were evaluated as a function of angle for the PM and the new PM + FM configurations by fitting data from NIST SRM640c Si powder. Peak shapes were easily modeled using pseudo-Voigt profiles and the peak widths follow a typical behavior with diffraction angle [17]. Figure 6 shows the FWHM as a function of angle fitted with a parabolic function, which suggests that the dual multilayer optics result in well-behaved line shapes and widths.

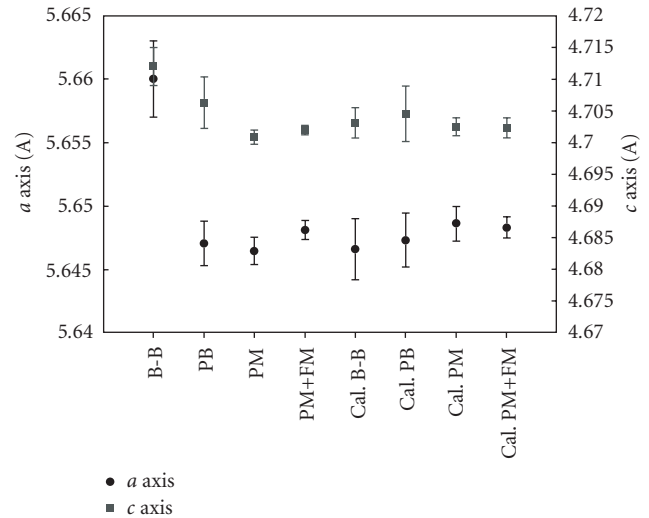


FIGURE 7: Refined lattice constants for urea for each instrumental configuration. Error bars are  $\pm 3$  estimated standard deviations from the refinements.

## 3.5. $2\Theta$ accuracy and precision

### 3.5.1. Traditional lattice parameter refinement

Refined lattice parameters, estimated standard deviations of the lattice parameters, and figures of merit are all good indicators for accuracy and precision when coupled with NIST certified standards [16]. To compare the diffractometer configurations, each powder was measured with an internal  $2\Theta$  standard, NIST 640b silicon powder. Lattice parameters were then refined from the data *without* calibrating the peak positions and then again *after* calibrating the peak positions (also called “internal standard  $2\Theta$  calibration”). In addition, the NIST standards 640c and 660 were measured independently. The results are summarized in Tables 2 and 3, with estimates of error that are the estimated standard deviation values from the multivariable refinement.

TABLE 3: Refined lattice parameters using internal standard calibrated data.

Material/configuration	$a$ axis (Å)	$c$ axis (Å)	No. of peaks indexed	Smith/Snyder $F_N$	No. of ESD from calibrated BB ( $a$ axis/ $c$ axis)	
Ag BB	4.08657(12)		8	$f(8) = 128$ (0.0078, 8)	0.0	
Ag PB	4.08618(41)		8	$f(8) = 32$ (0.0309, 8)	0.95	
Ag PM	4.08632(14)		8	$f(8) = 71$ (0.0141, 8)	1.79	
Linde C BB	4.75922(15)	12.9925(7)	31	$f(30) = 53$ (0.0125, 45)	0.00	0.00
Linde C PB	4.75810(2)	12.9893(9)	29	$f(29) = 55$ (0.0116, 45)	1.67	3.52
Linde C PM	4.75854(13)	12.9931(6)	30	$f(30) = 45$ (0.0148, 45)	4.53	0.89
Urea BB	5.6466(8)	4.7031(8)	21	$f(21) = 14$ (0.0294, 48)	0.00	0.00
Urea PB	5.6473(7)	4.705(1)	19	$f(19) = 24$ (0.0248, 32)	0.875	1.9
Urea PM	5.6486(5)	4.7025(5)	18	$f(18) = 74$ (0.0076, 32)	2.5	0.75

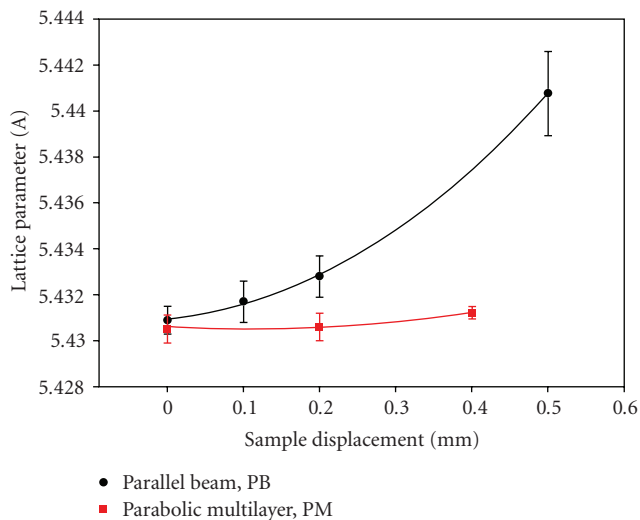


FIGURE 8: Lattice constants for SR640b silicon powder as a function of intentional specimen displacement for two configurations.

The principal source of error in peak positions from Bragg-Brentano diffractometers is the sample, and it is well known that the Bragg-Brentano para-focusing geometry is highly prone to sample displacement and sample transparency errors [16, 17]. The former results in systematic peak shifts while the latter results in asymmetric peak shapes. The use of a parallel beam on both the incident and diffracted beam sides of the sample eliminates, in principle, sample displacement and transparency errors. Likewise, using grazing angles ( $\Theta < 3^\circ$ ) reduces transparency errors by minimizing beam penetration into the sample. The lattice parameters obtained using the “parallel” optics, PB, PM, and PM + FM configurations, are therefore expected to yield the highest accuracy lattice parameters.

Assuming that the “correct” value for any particular lattice constant is the value determined from internal standard calibrated BB data, one can compare results for the various samples with different absorption coefficients in Tables 2 and 3. Examination of Tables 2 and 3 shows that, with one exception (the  $a$  axis of Linde C alumina), all

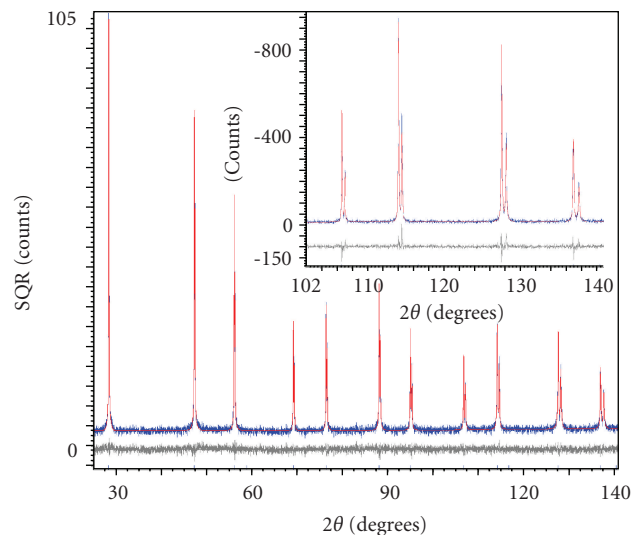


FIGURE 9: Rietveld plot for SRM640c Si on a square root scale. Inset shows high angle region on a linear scale.

of the lattice constants from *uncalibrated* data agree within error with the “ideal” value from calibrated Bragg-Brentano data. In contrast, all of the BB data and most of the PB data are significantly different from calibrated BB data. After calibration, the results are generally in agreement with the calibrated BB data, as expected.

One point of note relates to the low absorption specimen, urea. Urea manifests massive sample transparency error, with highly anisotropic line shapes even at intermediate diffraction angles in para-focusing geometry. Indeed, as shown in Figure 7, the transparency error is so large that the BB measurement provides substantially incorrect lattice constants but the “parallel” measurements are largely immune to sample transparency error. This point is visually obvious from the data in Figure 2.

### 3.5.2. Evaluation of sensitivity to specimen displacement

To evaluate the tolerable amount of displacement for the parallel beam configurations, samples of SRM 640b silicon were

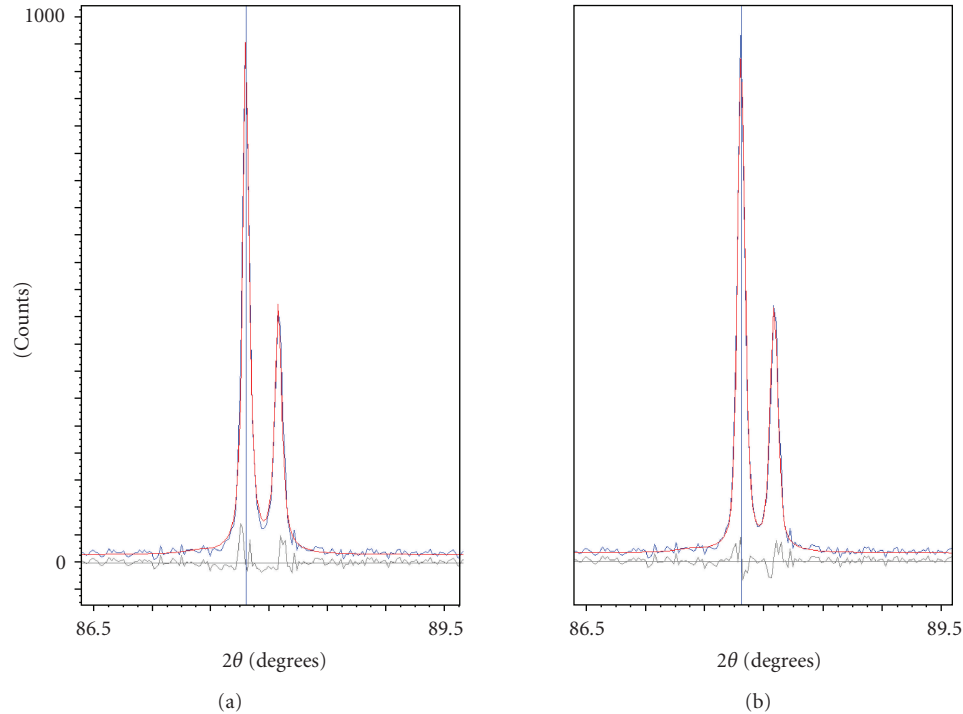


FIGURE 10: Profiles fit to SRM660a  $\text{LaB}_6$  using fundamental parameters: (a) is without an additional constant Gaussian convolution; (b) includes the constant Gaussian.

intentionally displaced from the diffractometer center by up to 0.5 mm. Although 0.5 mm is an extreme displacement, it is not uncommon for high temperature systems to introduce sample shifts [2, 13, 18] or for curved or rough surfaces to present large sample shifts, for example in residual stress analysis.

Figure 8 shows the lattice constants obtained for samples displaced from the goniometer center, and clearly demonstrates that the PM (and PM + FM, not shown) configuration is essentially immune to systematic sample displacement errors. The PB configuration has beam divergence 540 arcseconds on both sides of the sample, while the PM system has divergence of  $\sim 100$  arcseconds and 540 arcseconds on the incident and diffracted sides. Therefore, it appears that the largest divergence that can be tolerated while effectively eliminating sample displacement errors is somewhere between  $\sim 100$  and 500 arcseconds, which is unlikely to be achieved without a diffractive optical element—either a crystal or multilayer.

A final set of experiments focused on absolute accuracy using NIST Standard Reference Materials and the novel optical configuration of combined parabolic and flat multilayers. NIST SRM640c Si powder and the SRM1976 alumina plate were measured, both of which have certified lattice constants. Lattice parameter refinements for both materials resulted in unprecedented internal consistency, based upon the Smith-Snyder figure of merit ( $F_N$ ). For SRM640c, the lattice constant refined to within  $0.0006 \text{ \AA}$  of the certified value, with  $F_N = 521 (0.0019, 8)$ . Likewise, the data for SRM1976 refined to produce a very high  $F_N = 213$

(0.0026, 33), with the lattice constants within  $0.0007 \text{ \AA}$  of the certified value. These  $F_N$  values are enormous for any optical geometry, and very unusual for a laboratory instrument.

### 3.5.3. Rietveld refinement

Rietveld analysis of powder data from each configuration was performed using traditional pseudo-Voigt profiles and fundamental parameters peak shapes. Refinement of data from the PM and PM+FM configurations did not demonstrate any measurable abnormalities in the  $\alpha_1$  and  $\alpha_2$  peak positions. Refined models for alumina,  $\text{LaB}_6$ , and Si were all reasonable, including isotropic atomic displacement parameters. For example, the displacement parameters for Si powder were 0.37(1) for the PM configuration and 0.42(1) for the PM + FM configuration. Figure 9 shows the refined data for SRM640c in the PM + FM configuration.

The set of refinements using fundamental parameters line shapes also provided reasonable structure models, and the refined lattice constants from the PM and PM + FM configurations for the NIST standards were within  $0.0006 \text{ \AA}$  of the certified values. To optimize the fundamental parameters models for the PM and PM + FM configurations, the data were modeled without full structures using Pawley or individual profile fitting. The refinements included models for the axial and equatorial divergences and then additional convolutions to accommodate the multilayers [19]. Additional convolutions with refinable parameters included hat (square wave) and constant Gaussian functions.

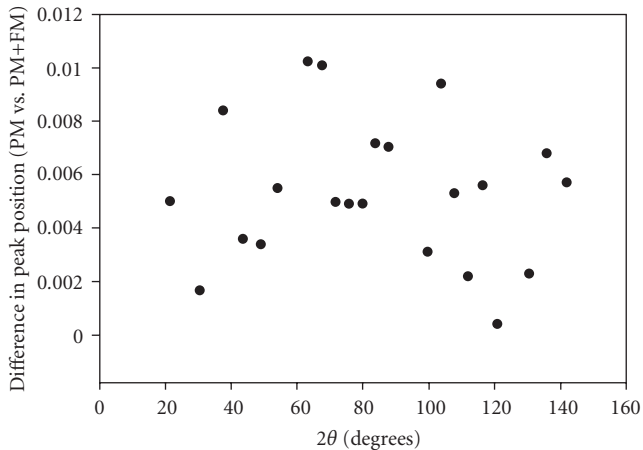


FIGURE 11: Difference in peak locations after deconvolution of the instrumental effects for SRM660a between the PM and PM + FM configurations after modeling with fundamental parameters.

For the PM + FM configuration, adding a constant Gaussian convolution notably improved the fit from  $Rwp = 19.5$  to  $16\%$ , a difference that is visible by eye as shown in Figure 10. In the case of the PM optical configuration, addition of both a constant hat function and a constant Gaussian function improved the model fits to the line profiles significantly, reducing  $Rwp$  from  $13.3$  to  $7\%$ . The Gaussian convolutions added to both models refined to nearly the same values,  $0.0440(5)$  for the system with two multilayers and  $0.041(1)$  for the single multilayer, suggesting that the incident beam parabolic multilayer contributes the Gaussian component to the line shapes. The hat function is a result of the long soller collimator and is absent in the case of two multilayers, presumably because the angular acceptance for the flat multilayer is some 5.5 times smaller than that of the parallel slit collimator. We are currently studying the effects of axial divergence and beam dimensions in the axial and equatorial directions to better define the convolutions.

After removing the instrumental effects from the peak locations using the fundamental parameters approach, the peak positions can be compared directly. Figure 11 shows the difference in peak location after deconvolution of the instrumental effects and shows a shift in zero error between the PM and PM + FM measurements of  $\sim 0.005^\circ 2\theta$ . Beyond the zero shift, however, the peak locations from the two configurations are within about  $\pm 0.004^\circ 2\theta$ , which is on the order of the reproducibility of the standard commercial goniometer used in the study (i.e.,  $\pm 0.003^\circ 2\theta$ , without encoders [20]). This result demonstrates that the two configurations are modeled correctly by incorporating the additional convolutions during fundamental parameters fitting.

#### 4. Summary

The novel configuration incorporating parabolic and flat multilayers is effective for powder diffraction measurements. Using only a parabolic multilayer on the incident beam

side resulted in all of the advantages expected from a parallel-beam system, and improved the measured intensity while maintaining the same peak-to-background ratio as the Bragg-Brentano configuration. Adding the flat multilayer in the diffracted beam side reduced the overall intensity but improved the resolution appreciably, as might be expected from the lower overall equatorial beam divergence. Systematic shifts in the  $\alpha_1$  and  $\alpha_2$  peak separations were not observed in the configurations tested, and the refined lattice constants for a range of materials were reasonable. Measurements of NIST SRM660, 660a, SRM1976, and SRM640c showed that the multilayers do not adversely affect the peak width versus angle, and provide refined lattice constants within  $0.0006 \text{ \AA}$  of the certified values in the worst case.

Fundamental parameters fitting of the line shapes demonstrated that the incident parabolic multilayer adds a Gaussian convolution (constant versus angle) to the line shape, which is the same for both the PM and PM+FM configurations. The long soller collimator on the diffracted beam side is best described using a constant hat function. The secondary flat mirror as an analyzer crystal does not alter the peak shapes appreciably, so that the line shapes from the system with two multilayers can be modeled with only the constant Gaussian function.

#### Acknowledgments

The author is indebted to Arnt Kern of Bruker AXS, Wis, USA, for providing the *Topas* software and Alan Coelho for valuable discussions and modeling some data using *Topas*.

#### References

- [1] R. D. Deslattes, J. L. Staudenmann, L. T. Hudson, A. Henins, and J. P. Cline, "Parallel beam powder diffraction using a laboratory X-ray source," *Advances in X-Ray Analysis*, vol. 41, pp. 221–231, 1997.
- [2] M. D. Dolan, S. Zdziszynski, and S. T. Misture, "A high-temperature powder diffraction furnace," *Advances in X-Ray Analysis*, vol. 46, pp. 50–55, 2003.
- [3] G. Gutman and B. Verman, "Calculation of improvement to HRXRD system through-put using curved graded multilayers," *Journal of Physics D*, vol. 29, no. 6, pp. 1675–1676, 1996.
- [4] S. T. Misture, "Rietveld refinement of powder data from multilayer optics," *Advances in X-Ray Analysis*, vol. 45, pp. 166–171, 2002.
- [5] S. T. Misture, "Characterization of glass surfaces and coatings using X-ray reflectivity," *American Ceramic Society Bulletin*, vol. 83, no. 1, pp. 27–29, 2004.
- [6] N. A. Raferty and R. Vogel, "Limitations of asymmetric parallel-beam geometry," *Journal of Applied Crystallography*, vol. 37, part 3, pp. 357–361, 2004.
- [7] M. Schuster and H. Goebel, "Parallel-beam coupling into channel-cut monochromators using curved graded multilayers," *Journal of Physics D*, vol. 28, no. 4A, pp. 270–275, 1995.
- [8] M. Wohlschlögel, T. U. Schüllli, B. Lantz, and U. Welzel, "Application of a single-reflection collimating multilayer optic for X-ray diffraction experiments employing parallel-beam geometry," *Journal of Applied Crystallography*, vol. 41, part 1, pp. 124–133, 2008.

- [9] H. Toraya and H. Hibino, " $K\alpha_1$ - $K\alpha_2$  characteristic of a parabolic graded multilayer," *Journal of Applied Crystallography*, vol. 33, part 6, pp. 1317–1323, 2000.
- [10] G. Fujinawa and A. Sasaki, "Development of a high-resolution and high-accuracy parallel beam powder diffractometer using laboratory X-ray sources," *X-sen Bunseki no Shinpo*, vol. 31, pp. 11–27, 2000.
- [11] M. S. Haluska, S. A. Speakman, and S. T. Misture, "Crystal structure determinations of three-layer Aurivillius ceramics using a new parallel beam X-ray powder diffractometer," *Advances in X-Ray Analysis*, vol. 46, pp. 192–197, 2003.
- [12] C. Michaelsen, P. Ricardo, D. Anders, M. Schuster, J. Schilling, and H. Göbel, "Improved graded multilayer mirrors for XRD applications," *Advances in X-Ray Analysis*, vol. 42, pp. 308–320, 2000.
- [13] P. S. Whitfield, "Use of double Göbel mirrors with high-temperature stages for powder diffraction—a strategy to avoid severe intensity fade," *Journal of Applied Crystallography*, vol. 36, no. 2, part 3, pp. 926–930, 2003.
- [14] "X'Pert HighScore Plus," PANalytical B.V., 2006.
- [15] Diffrac Plus: TOPAS, "General Profile Structure and Analysis Software for Powder Diffraction Data," Bruker AXS, Karlsruhe, Germany, 2005.
- [16] R. Jenkins and R. L. Snyder, *Introduction to X-Ray Powder Diffractometry*, John Wiley & Sons, New York, NY, USA, 1996.
- [17] H. P. Klug and L. E. Alexander, *X-Ray Diffraction Procedures*, John Wiley & Sons, New York, NY, USA, 1974.
- [18] S. T. Misture, C. R. Hubbard, and X. L. Wang, "Systematic errors in metal strip diffraction furnaces," *Advances in X-Ray Analysis*, vol. 45, pp. 25–30, 2002.
- [19] R. W. Cheary and A. Coelho, "Fundamental parameters approach to X-ray line-profile fitting," *Journal of Applied Crystallography*, vol. 25, part 2, pp. 109–121, 1992.
- [20] R. W. Cheary, J. P. Cline, and M. Anast, "Characterisation and modelling of peak shifts in conventional powder diffractometry," *Advances in X-Ray Analysis*, vol. 39, pp. 579–587, 1997.